Available online at www.sciencedirect.com
SCIENCE DIRECT®
Journal of Computational Physics 211 (2006) 300–325
JOURNAL OF COMPUTATIONAL PHYSICS
www.elsevier.com/locate/jcp

Spectral element formulations on non-conforming grids: A comparative study of pointwise matching and integral projection methods ☆

Cuneyt Sert [a], Ali Beskok [b,*]

[a] *Mechanical Engineering Department, Middle East Technical University, Ankara 06531, Turkey*
[b] *Mechanical Engineering Department, Texas A&M University, College Station, TX 77843-3123, United States*

Received 30 November 2004; received in revised form 18 May 2005; accepted 27 May 2005
Available online 18 July 2005

Abstract

Pointwise matching (PM) and integral projection (IP) methods are two widely used techniques to extend the classical weak formulations to include non-conforming grids. We present spectral element formulations on polynomial (p-type) and geometric (h-type) non-conforming grids using both the PM (also known as the Constrained Approximation) and IP (also known as the Mortar Element) methods. We systematically compare the convergence characteristics of PM and IP methods for diffusion, convection, and convection–diffusion equations. Consistency errors due to the non-conforming formulations of the diffusion equation result in convergence problems for the PM method using the maximum rule. Both non-conforming formulations for the unsteady convection operator result in eigenvalue spectrum with positive real values, causing convergence problems due to the consistency errors. However, small ''physical'' diffusion in the convection–diffusion equation eliminates these problems, resulting in spectral convergence for both methods. Encouraged by this, we present spectral element formulations for incompressible Navier–Stokes equations using PM and IP methods on p-type and h-type non-conforming grids, and demonstrate spectral convergence for unsteady and steady test cases. Results for two-dimensional lid-driven cavity flow at $Re = 1000$ are also presented.

Keywords: Non-conforming elements; Spectral element method; Pointwise matching; Integral projection; Mortar element; Constrained approximation

☆ This paper is based on work first presented at the 4th European Congress on Computational Methods in Applied Sciences and Engineering, Jyväskylä, Finland, 2004.

* Corresponding author. Tel.: +1 979 862 1073.
E-mail address: abeskok@tamu.edu (A. Beskok).

0021-9991/$ - see front matter
doi:10.1016/j.jcp.2005.05.019

1. Introduction

Spectral element methods (SEM) are high-order domain decomposition methods [14,18,19] that combine the competitive advantages of low-order finite element (h-FEM) and high-order spectral methods. Finite element methods are attractive because of their highly flexible domain decomposition capability [20]. Spectral methods, on the other hand, are preferred because of their exponential convergence characteristics, and the built-in p-refinement capability [6,10].

SEM are multi-element methods, and similar to the FEM, their weighted-residual-based implementations often utilize conforming elements. By conformity we mean *matching of the collocation points* (points where the unknowns are calculated) *at element interfaces* (Fig. 1(a)). Conforming mesh usually results in severe restrictions on mesh refinements. For example, localized refinements by increasing the polynomial expansion order (p-refinements) often result in propagation of the high-order polynomial discretization to the entire domain. Non-propagating mesh refinements by dividing large elements into smaller elements (h-refinements) are not possible either, because no hanging vertices are allowed at the element interfaces. Efficient discretization of complex engineering geometries and proper resolution of the fine scale physics using spectral element methods require both h-type and p-type refinement techniques.

There are several ways to extend the classical conforming formulations to include non-conforming elements. One of the early methods is the Pointwise matching (also known as the Constrained Approximation) Method (PMM) [7,24]. It regains the lost C^0 continuity at the non-conforming interfaces by enforcing pointwise projection of the unknowns. Another method is the integral projection (Mortar Element) Method (IPM) [3,4,12,15]. In this method, C^0 continuity is not regained, however the jump at the non-conforming interfaces are minimized by enforcing a weighted-integral matching. Other methods that are utilized to handle the non-conformities include Zanoli Iteration Method [8], Transition Element Method [11] and Finite Element Tearing and Interconnecting Method [16].

In this paper, we study spectral element formulations for p-type and h-type non-conformities using the PMM and IPM. The p-type non-conformities are observed at the interface between two geometrically matching elements with different polynomial expansion orders. This results in non-matching collocation points at the common interface, as shown in Fig. 1(b). The h-type non-conformities include an interface of geometrically non-matching elements. For example, Fig. 1(c) shows the interface with a single hanging vertex, which is also known as the "1-irregular interface". Such interfaces are popular because they provide enough flexibility for most practical problems with minimum programming difficulty. PMM is the preferred method in finite element community, whereas IPM is mostly used with spectral element formulations. The literature studying these two methods together are very limited. In this paper, we present implementation and applications of PMM and IPM for diffusion, convection, convection–diffusion, and incompressible Navier–Stokes equations, and compare their performance on both h-type and p-type non-conforming grids.

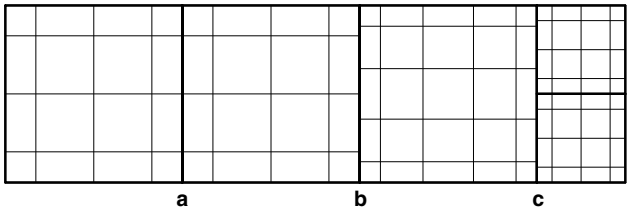

Fig. 1. Types of interfaces: (a) conforming, (b) p-type non-conforming, (c) h-type type non-conforming (thick lines in all four plots show element boundaries and intersection of thin lines show collocation points).

This paper is organized as follows. In Section 2, we present a review of the Galerkin spectral element formulation, which is followed by detailed discussions of the PMM and IPM formulations for both p-type and h-type non-conformities. In Sections 4 and 5, we present effects of non-conformities on the steady and unsteady diffusion, convection, and convection–diffusion equations. In Section 6, solutions of the incompressible Navier–Stokes test problems are presented. Finally, in Section 7, we summarize our findings and conclude.

2. Conforming Galerkin spectral element formulation

We will consider PMM and IPM as extensions to the conforming spectral element methods. Therefore, we start by summarizing the conforming Galerkin spectral element (GSE) formulation. Let us consider a two-dimensional Poisson problem and study its GSE formulation step-by-step.

Step 1 – Strong formulation. Find θ such that

$$-\nabla^2\theta = f \quad \text{on } \Omega, \tag{1a}$$

$$\theta = g \quad \text{on } \Gamma_g, \tag{1b}$$

$$n\cdot\nabla\theta = h \quad \text{on } \Gamma_h, \tag{1c}$$

where Ω is the problem domain and $\Gamma = \Gamma_g \cup \Gamma_h$ is the boundary of Ω. The unit normal n, points outward from boundary Γ_h, and f, g and h are known functions.

Step 2 – Weighted residual formulation. Define the residual of Eq. (1a) as

$$-\nabla^2\theta - f = 0 \tag{2}$$

and force the approximate solution to satisfy the residual equation in a weighted integral sense

$$\int_\Omega (-\nabla^2\tilde{\theta} - f) w \, \mathrm{d}\Omega = 0, \tag{3}$$

where the approximate solution $\tilde{\theta}$ and the weight function w belong to the appropriate space of piecewise polynomials.

Step 3 – Weak formulation. Apply integration by parts to the first term of Eq. (3)

$$\int_\Omega \nabla\tilde{\theta}\cdot\nabla w \, \mathrm{d}\Omega = \int_\Omega f w \, \mathrm{d}\Omega + \oint_{\Gamma_h} h w \, \mathrm{d}s. \tag{4}$$

Step 4 – Domain discretization. Divide domain Ω into subdomains (elements) Ω^e and apply the weak formulation in each subdomain individually

$$\int_{\Omega^e} \nabla\tilde{\theta}^e\cdot\nabla w^e \, \mathrm{d}\Omega^e = \int_{\Omega^e} f^e w^e \, \mathrm{d}\Omega^e + \oint_{\Gamma_h^e} h^e w^e \, \mathrm{d}s^e. \tag{5}$$

Step 5 – Element discretization. Discretize each element further by $M\times N$ collocation points and express the discretized form of θ as

$$\tilde{\theta}(\xi,\eta) = \sum_{m=0}^{N}\sum_{n=0}^{M} \tilde{\theta}^e_{mn} l^M_m(\xi) l^N_n(\eta) = \sum_{j=1}^{ncp} \tilde{\theta}^e_j S_j(\xi,\eta), \tag{6}$$

where $ncp = (M + 1)(N + 1)$ is the number of collocation points in element e. ξ and η are the axes of the two-dimensional master element. S_j is the two-dimensional shape function associated with point j, which is the tensor product of one-dimensional Lagrange interpolants l_m^M and l_n^N defined on Gauss–Lobatto–Legendre (GLL) collocation points. l_m^M and l_n^N are Mth- and Nth-order polynomials, respectively, and they are defined as:

$$l_m^M(\xi) = -\frac{(1-\xi^2)P'_M(\xi)}{M(M+1)P_M(\xi_m)(\xi-\xi_m)}, \quad m \in [0, M], \tag{7}$$

where P_M and P'_M are the Mth-order Legendre polynomial and its derivative, respectively [14].

Step 6 – Weight function selection. In the Galerkin formulation weight function w is selected to be the same as the shape functions used for the unknown

$$w = S_i, \quad i \in [1, ncp]. \tag{8}$$

Step 7 – Elemental matrix form. Substitute Eqs. (6) and (8) into Eq. (5) to obtain

$$\int_{\Omega^e} \sum_{j=1}^{ncp} \tilde{\theta}_j^e \nabla S_j \cdot \nabla S_i \, \mathrm{d}\Omega^e = \int_{\Omega^e} f^e S_i \, \mathrm{d}\Omega^e + \oint_{\Gamma_h^e} h^e S_i \, \mathrm{d}s^e, \tag{9}$$

which can be put into the following elemental matrix form:

$$[K]^e\{\tilde{\theta}\}^e = \{\bar{f}\}^e + \{Q\}^e = \{f\}^e, \tag{10}$$

where $[K]^e$ and $\{f\}^e$ are the elemental stiffness matrix and force vector, respectively.

Step 8 – Assembly. Elemental matrices for each element is assembled to form a global system of algebraic equations.

$$[K] = \sum_{e=1}^{ne} [K]^e, \quad \{f\} = \sum_{e=1}^{ne} \{f\}^e. \tag{11}$$

It is worth to note that the conformity between the element interfaces is implicitly used during the assembly process, which needs a one-to-one matching between the unknowns of the elements sharing an interface (Fig. 1(a)). The modified assembly process is required for non-conforming elements will be demonstrated in the next section.

3. Formulations on non-conforming grids, PMM and IPM

In this section, we present the details of PMM and IPM algorithms. In the coming subsections, we demonstrate the principles of both techniques on p-type and h-type non-conforming interfaces. The following discussion is intended to be implementation oriented rather than being mathematically rigorous. Each method is studied sequentially using step-by-step instructions, which enables a better comparison between them.

3.1. Pointwise matching method (PMM)

PMM is a method where we regain the C^0 continuity that is lost at the non-conforming interfaces. This is done by a pointwise projection and matching of the unknowns of one face to the other. We will demonstrate this method using the simple configuration given at Fig. 2, which shows a 3rd order element

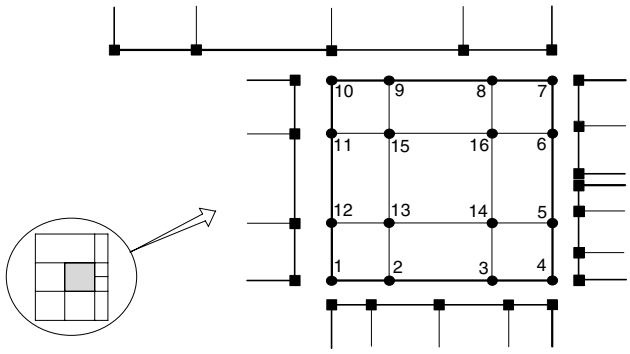

Fig. 2. An element with $M = N = 3$rd order expansion and $ncp = 16$ collocation points. Faces shared with five neighboring elements are also shown. South interface has p-type, East and North interfaces have h-type non-conformities. West interface is conforming. Points of the center element and the neighboring faces are shown with circles and squares, respectively.

($M = N = 3$) surrounded by five neighbors. Only the faces of the neighbors' that are shared with the middle elements are shown. The formulation explained below is based on the work of Chang and Hsu [7].

Step 1 – Determine the non-conforming interfaces and type of non-conformities. In our example South interface has p-type, East and North interfaces have h-type non-conformities. West interface is conforming.

Step 2 – Decide on active and passive faces. At the non-conforming interfaces collocation points of two neighboring faces are not matching (circles are not matching with squares). Both sets of points cannot be used in the assembly process. A decision should be made on which set of points to be used. These points will be called *active points* and remaining set of points will be called *passive points*. Let us first concentrate on the South interface where we have p-type non-conformity. There are two possibilities in determining the active/passive faces. First one is known as the *minimum rule*: Face with lower expansion order is the active face. The other possibility is the *maximum rule* which is just the opposite of the minimum rule. For this illustration maximum rule will be used. Now let us look at the East and North interfaces, where we have h-type non-conformities. This time there is only one choice, which we call the *long rule*: Longer face is the active face and two shorter faces are the passive faces. Later it will be clear why the other possibility, the *short rule* is not preferred with PMM.

Step 3 – Generate the constrained element. Fig. 3(a) shows the original element whose (according to the above discussion) South and North faces are passive. Fig. 3(b) shows the constrained element obtained by replacing the points on the passive faces of the original element by the points of the active neighboring faces. Deleted points of the original element (2, 3, 8, 9) are the passive points. By definition all the points of the constrained element are the active points. These are the points that will go into the assembly process.

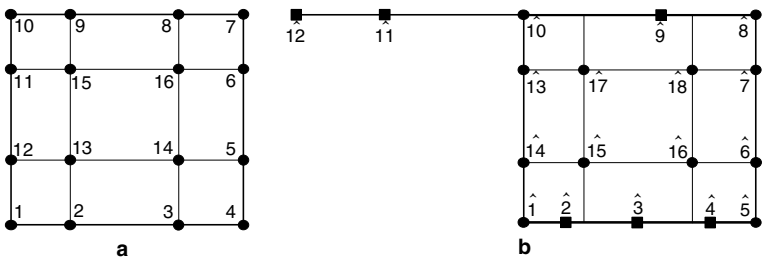

Fig. 3. PMM: (a) original element with $ncp = 16$ and (b) constrained element with $\widehat{ncp} = \hat{18}$.

Step 4 – Write the unknowns at the passive points in terms of the unknowns at the active points. This is the key step which is different for each non-conforming technique. PMM is one of the easiest ones, in which we enforce a projection of unknowns at the passive points onto the active faces. Let us concentrate on the South face. We want to write the unknowns at the passive points 2 and 3 in terms of the unknowns at the active points $\hat{1}$–$\hat{18}$. For this purpose, Eq. (6) can be used on the constrained element. For example, at point 2 (~ is dropped for the sake of clarity),

$$\theta_2 = \sum_{\hat{j}=\hat{1}}^{\widehat{ncp}} \theta_j^e S_{\hat{j}}(\xi_2, \eta_2). \tag{12}$$

Note that point 2 is on a face, hence two-dimensional shape functions reduce to one-dimensional Lagrange interpolants. Using this fact, Eq. (12) can be simplified to

$$\theta_2^e = \theta_{\hat{1}}^e l_{\hat{1}}(\xi_2) + \theta_{\hat{2}}^e l_{\hat{2}}(\xi_2) + \theta_{\hat{3}}^e l_{\hat{3}}(\xi_2) + \theta_{\hat{4}}^e l_{\hat{4}}(\xi_2) + \theta_{\hat{5}}^e l_{\hat{5}}(\xi_2). \tag{13}$$

This is called the constraint approximation for the passive point 2. A similar equation can be written for point 3, and together they can be expressed in the following vector equation:

$$\begin{Bmatrix} \theta_2 \\ \theta_3 \end{Bmatrix}^e = [C_S]^e \begin{Bmatrix} \theta_{\hat{1}} \\ \theta_{\hat{2}} \\ \theta_{\hat{3}} \\ \theta_{\hat{4}} \\ \theta_{\hat{5}} \end{Bmatrix}^e = \begin{bmatrix} l_{\hat{1}}(\xi_2) & l_{\hat{2}}(\xi_2) & l_{\hat{3}}(\xi_2) & l_{\hat{4}}(\xi_2) & l_{\hat{5}}(\xi_2) \\ l_{\hat{1}}(\xi_3) & l_{\hat{2}}(\xi_3) & l_{\hat{3}}(\xi_3) & l_{\hat{4}}(\xi_3) & l_{\hat{5}}(\xi_3) \end{bmatrix}^e \begin{Bmatrix} \theta_{\hat{1}} \\ \theta_{\hat{2}} \\ \theta_{\hat{3}} \\ \theta_{\hat{4}} \\ \theta_{\hat{5}} \end{Bmatrix}^e, \tag{14}$$

where C_S is the conformity matrix for the South face. A similar equation can be written for the passive points of the North face,

$$\begin{Bmatrix} \theta_8 \\ \theta_9 \end{Bmatrix}^e = [C_N]^e \begin{Bmatrix} \theta_{\hat{8}} \\ \theta_{\hat{9}} \\ \theta_{\hat{10}} \\ \theta_{\hat{11}} \\ \theta_{\hat{12}} \end{Bmatrix}^e = \begin{bmatrix} l_{\hat{8}}(\xi_8^*) & l_{\hat{9}}(\xi_8^*) & l_{\hat{10}}(\xi_8^*) & l_{\hat{11}}(\xi_8^*) & l_{\hat{12}}(\xi_8^*) \\ l_{\hat{8}}(\xi_9^*) & l_{\hat{9}}(\xi_9^*) & l_{\hat{10}}(\xi_9^*) & l_{\hat{11}}(\xi_9^*) & l_{\hat{12}}(\xi_9^*) \end{bmatrix}^e \begin{Bmatrix} \theta_{\hat{8}} \\ \theta_{\hat{9}} \\ \theta_{\hat{10}} \\ \theta_{\hat{11}} \\ \theta_{\hat{12}} \end{Bmatrix}^e, \tag{15}$$

where

$$\xi_8^* = \frac{\xi_8 + 1}{2}, \quad \xi_9^* = \frac{\xi_9 + 1}{2}$$

are used in order to project the coordinates of the North face of the original element (ξ) onto the neighboring face (ξ^*) properly. It is also clear from this projection why the *short rule* is not used with PMM. Because that would yield terms in C_N like $l_i(\xi_j^*)$ $(i = 7, 8, 9, 10, j = 11, 12)$ which are not defined (l_i (i = 7, 8, 9, 10) are defined only in $0 < \xi^* < 1$).

Now unknowns at all four passive points (2, 3, 8, 9) are expressed in terms of the unknowns at the active points.

Step 5 – Setup the elemental conformity matrix. Note that there is one-to-one matching of many points of the original and constrained elements. Using these matchings and the previously defined C_S and C_N, an elemental conformity matrix can be assembled to relate the unknowns of the original element to the unknowns of the constrained element.

$$\{\theta\}^e = [C]^e\{\hat{\theta}\}^e, \quad \text{where } [C]^e = \begin{bmatrix} 1 &&&&&&&&&&&&&&&&& \\ \bullet & \bullet & \bullet & \bullet & \bullet &&&&&&&&&&&&& \\ \bullet & \bullet & \bullet & \bullet & \bullet &&&&&&&&&&&&& \\ &&&& 1 &&&&&&&&&&& 0 && \\ &&&&& 1 &&&&&&&&&&&& \\ &&&&&& 1 &&&&&&&&&&& \\ &&&&&&& 1 &&&&&&&&&& \\ &&&&&&& \bullet & \bullet & \bullet & \bullet & \bullet &&&&&& \\ &&&&&&& \bullet & \bullet & \bullet & \bullet & \bullet &&&&&& \\ &&&&&&&&& 1 &&&&&&&& \\ &&&&&&&&&&&& 1 &&&&& \\ &&&&&&&&&&&&& 1 &&&& \\ &&& 0 &&&&&&&&&&& 1 &&& \\ &&&&&&&&&&&&&&& 1 && \\ &&&&&&&&&&&&&&&& 1 & \\ &&&&&&&&&&&&&&&&& 1 \end{bmatrix}_{ncp\times n\hat{c}p} \tag{16}$$

and $\{\hat{\theta}\}$ represents the unknowns of the constrained element. As seen from this equation, elemental conformity matrices are very sparse. This is because only the face points are affected by the constraint functions. Unity entries are due to one-to-one matching points of the original and constrained elements. Non-unity entries coming from C_S and C_N are shown with dots.

Step 6 – Modified assembly process. After setting up the elemental conformity matrices for each element, these can be used in the modified assembly

$$[K] = \sum_{e=1}^{ne}[C]^{e\text{T}}[K]^e[C]^e, \quad \{f\} = \sum_{e=1}^{ne}[C]^{e\text{T}}\{f\}^e. \tag{17}$$

Here, it is very important to note that up to the assembly process having non-conformities does not make any difference. Elemental stiffness matrices and force vectors are constructed using original elements as if there were no non-conformities. Therefore, PMM requires very little programming and computational overhead due to the non-conformities. The challenge is the design and efficient management of elemental data, which is less organized compared to a conforming mesh.

3.2. Integral projection method (IPM)

Unlike PMM, IPM does not regain the lost C^0 continuity at the non-conforming interfaces via pointwise projection. Instead, it minimizes the jump across such interfaces in a weighted integral sense. Again we will end up with elemental conformity matrices and use them to modify the assembly process. However, the numerical values of these matrices and the way they are obtained are different. Following the formulation given by Bernardi et al. [3,4], we demonstrate the details of IPM using the mesh configuration of Fig. 2.

Step 1 – Determine the non-conforming interfaces and type of non-conformities. Same as the first step of PMM.

Step 2 – Decide on active and passive faces. At p-type non-conforming South interface again there is the freedom to choose either the minimum or the maximum rule. Let us again choose the maximum rule. At h-type non-conforming East and North interfaces there are two possibilities, short and long rules. Here, the short rule will be used, reasons of which will be explained later.

Step 3 – Generate the constrained element. Fig. 4(a) shows the original element. According to the selections made in the second step, its' South and East faces are passive. Fig. 4(b) shows the constrained element obtained by replacing the points on the passive faces of the original element by the points of the active neighboring faces. Therefore this time, passive points are 2, 3, 5, 6, and again all the points of the constrained element are active. In the following discussion, at a p-type non-conforming interface, expansion orders of the passive and active faces will be denoted by N_1 and N_2, respectively. Therefore for the South face of our example $N_1 = 3$, $N_2 = 4$. At an h-type interface, expansion order of the long face will be denoted by N_1 and expansion orders of the two small faces by N_2 and N_3. For our example's, East face $N_1 = 3$, $N_2 = 3$, $N_3 = 2$.

Step 4 – Write the unknowns at the passive points in terms of the unknowns at the active points. This step is different than the fourth step of PMM. Let us first work on the South face. We want to write the unknowns at the passive points 2 and 3 in terms of the unknowns at the active points. This time the constraint functions will not enforce a pointwise matching but rather a weaker matching. We will take a weighted line integral at the South face of the original element,

$$I_1 = \oint_{1-4} \theta \psi_i \, \mathrm{d}s, \tag{18}$$

where ψ_i is the weight function associated with the ith passive point. In order to get two equations for unknowns at the two passive points (2 and 3), two weight functions are necessary. They are usually selected to be modified GLL-based Lagrange interpolants that are two order less than the order of the original face.

$$\psi_i = (-1)^{N_1 - i} \frac{L'_{N_1}(\xi)}{\xi_i - \xi}, \quad i = 1, \ldots, N_1 - 1. \tag{19}$$

Two orders less, because the end point conditions ($\theta_1 = \theta_{\hat{1}}, \theta_4 = \theta_{\hat{5}}$) removes two degrees of freedom from the constraint at each passive face. Using the discretized form of the unknown θ from Eq. (6) (dropping $\sim$ for the sake of clarity), Eq. (18) becomes

$$I_1 = \sum_{j=1}^{4} \oint_{1-4} \theta_j l_j \psi_i \, \mathrm{d}s. \tag{20}$$

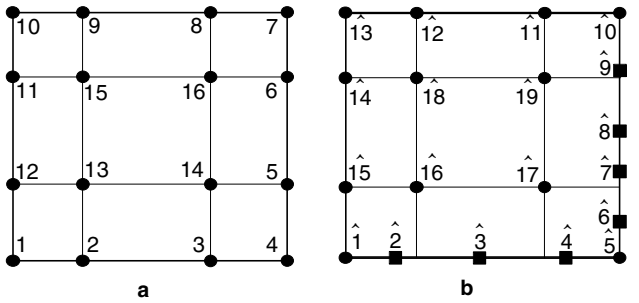

Fig. 4. IPM: (a) original element with $ncp = 16$ and (b) constrained element with $n\hat{c}p = \hat{19}$.

Note that the summation includes only the points of the South face. There will be no contribution from other points because shape functions associated with those points have zero value at the South face. Also note that two-dimensional shape functions reduce to one-dimensional Lagrange interpolants at the faces. Now let us take a similar line integral but this time at the South face of the constrained element

$$I_2 = \sum_{\hat{j}=\hat{1}}^{\hat{5}} \oint_{\hat{1}-\hat{5}} \theta_{\hat{j}} l_{\hat{j}} \psi_i \, \mathrm{d}s. \tag{21}$$

Constraint functions for IPM can be obtained by equating I_1 and I_2,

$$\sum_{j=1}^{4} \oint_{1-4} \theta_j l_j \psi_i \, \mathrm{d}s = \sum_{\hat{j}=\hat{1}}^{\hat{5}} \oint_{\hat{1}-\hat{5}} \theta_{\hat{j}} l_{\hat{j}} \psi_i \, \mathrm{d}s. \tag{22}$$

Using GLL quadrature for the integrals and the two end-point conditions, this system can be reduced to

$$[B_S] \begin{Bmatrix} \theta_2 \\ \theta_3 \end{Bmatrix}^e = [P_S] \begin{Bmatrix} \theta_{\hat{1}} \\ \theta_{\hat{2}} \\ \theta_{\hat{3}} \\ \theta_{\hat{4}} \\ \theta_{\hat{5}} \end{Bmatrix}^e \quad \Rightarrow \quad \begin{Bmatrix} \theta_2 \\ \theta_3 \end{Bmatrix}^e = [C_S] \begin{Bmatrix} \theta_{\hat{1}} \\ \theta_{\hat{2}} \\ \theta_{\hat{3}} \\ \theta_{\hat{4}} \\ \theta_{\hat{5}} \end{Bmatrix}^e, \tag{23}$$

which has the same form as Eq. (14) derived for PMM. Of course the entries of the conformity matrix $[C_S]$ of the South face are different, and they depend on the order of the GLL quadrature used for the integrals, I_1 and I_2. From Eq. (20), it can be seen that I_1 includes polynomials of order $(N_1 + N_1 - 2)$, which can be calculated exactly with N_1th-order GLL quadrature (Nth-order GLL quadrature can evaluate $(2N - 1)$th-order polynomials exactly). Also using N_1th-order quadrature yields a diagonal B_S matrix, which eliminates the matrix inversion of Eq. (23). I_2, on the other hand, has polynomials of order $(N_1 + N_2 - 2)$, which can be calculated exactly using a GLL quadrature of order $N = \max(N_1, N_2)$.

East interface, which has h-type non-conformity, requires a similar procedure to calculate the conformity matrix C_E. Skipping the details [22], this time there are three line integrals. I_1 is evaluated on the East face of the original element. I_2 and I_3 are evaluated on the two small active neighboring faces. Constraint functions necessary for the passive points 5 and 6, are then obtained by $I_1 = I_2 + I_3$. As discussed for PMM, special attention is necessary in the proper projection of coordinates at the active faces onto the passive face, since they are not geometrically matching (see [3,22] for details). At this point one can understand why the short formulation is not suitable for IPM. Short formulation for IPM would require the evaluation of weight functions ψ based on short faces at the collocation points of a long face, which is cumbersome.

Steps 5 and 6 are identical to that of the PMM.

As demonstrated in the last two sections, formulation of PMM and IPM end up modifying the classical Galerkin formulation in very similar ways. However, they do not always perform equally well. In the following sections, we will compare the convergence and eigenvalue characteristics of these two methods using diffusion, convection, and convection–diffusion equations.

4. Diffusion equation

Consider the following two-dimensional steady diffusion equation with Dirichlet boundary conditions

$$-\nabla^2\theta = f \quad \text{on } \Omega \in [0,1]\times[0,1], \tag{24a}$$

$$\theta = \theta_{\text{exact}} \quad \text{on } \Gamma. \tag{24b}$$

The force function is selected such that the exact solution is

$$\theta_{\text{exact}} = \sin(4\pi\sqrt{(x-2)^2+(y-2)^2}). \tag{25}$$

We will solve this problem using two different meshes shown in Figs. 5(a) and (b).

4.1. Test 1: spectral convergence on a conforming mesh

First we will utilize a fully conforming mesh (shown in Fig. 5(a)) to demonstrate the spectral convergence upon p-type refinement. Expansion orders of $N = N_1 = N_2$ will be used, where N_i denotes the expansion order of the ith element in both x- and y-directions. The thick line in Fig. 6 shows the convergence plot (maximum error vs. expansion order) for this test. For sufficiently smooth problems, such as given in this case, SEM results in exponential decay of discretization errors by increasing the elemental expansion order N (straight line on a log–lin plot) [6].

4.2. Test 2: convergence on a p-type non-conforming mesh

In this test, convergence of PMM and IPM is compared on a p-type non-conforming mesh. The same two-element mesh is used, but this time a p-type non-conformity is introduced by varying the expansion orders in the y-direction. The expansion order in the x-direction for both elements are kept constant at 16. This is a high enough value to ensure that the errors are dominated by the discretization in the y-direction, along which the non-conformity lies.

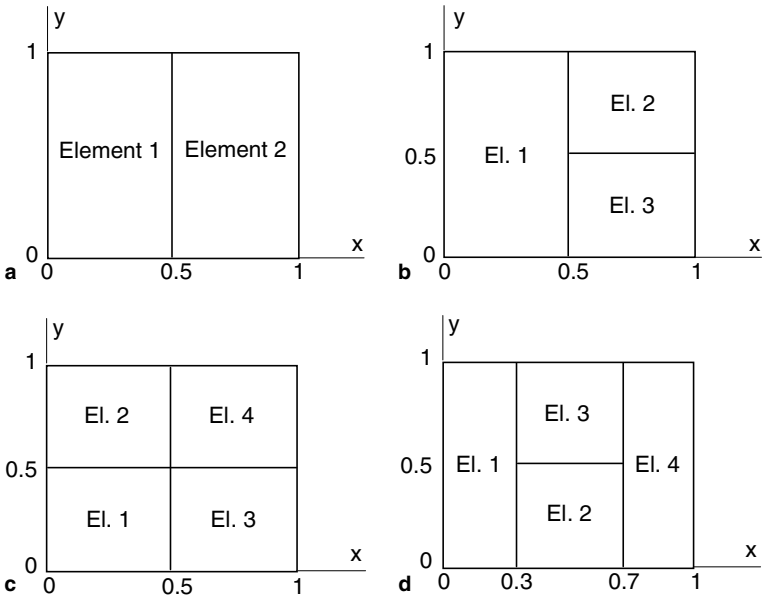

Fig. 5. Various meshes with geometrically conforming and non-conforming elements.

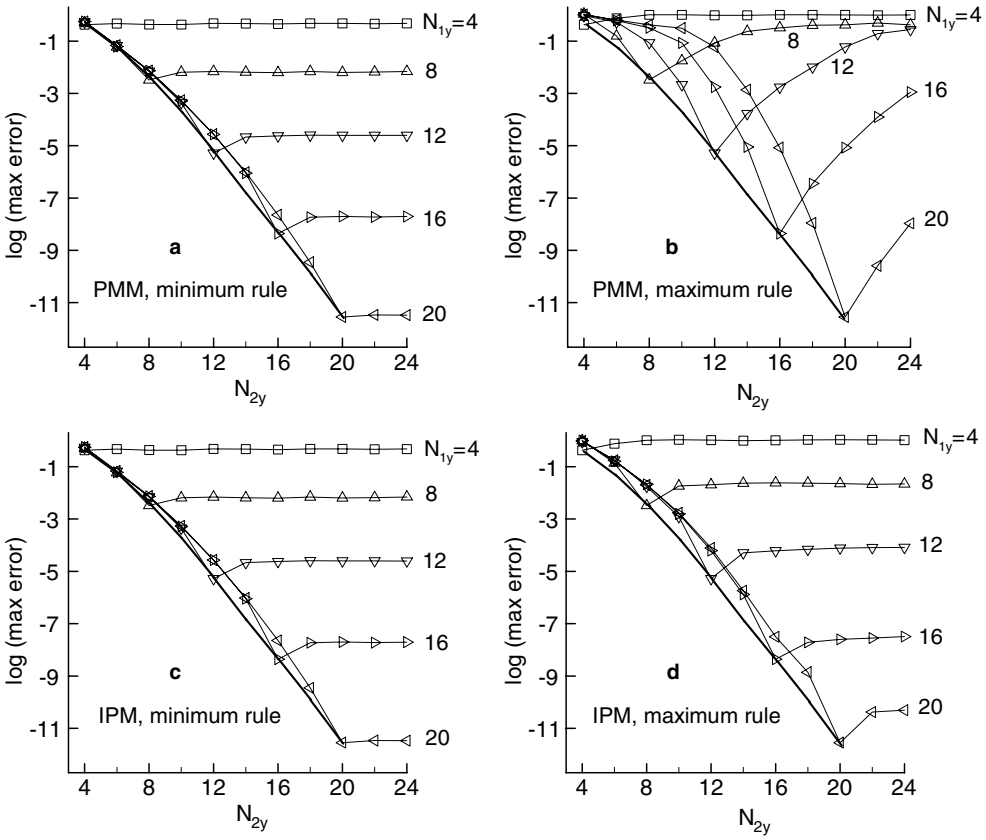

Fig. 6. Convergence curves obtained for the diffusion equation (Tests 1 and 2). Thick lines are identical and correspond to the conforming case of Test 1. Test 2 uses two-element *p-type non-conforming mesh* with combinations of: (a) PMM, minimum rule (b) PMM, maximum rule, (c) IPM, minimum rule and (d) IPM, maximum rule.

Fig. 6 shows the maximum errors obtained by different combinations of N_{1y} and N_{2y}. Combinations of PMM, IPM, and minimum, maximum rules are shown as separate plots. The thick lines of each plot are identical and correspond to the conforming case. Let us study these plots by concentrating on the convergence curve for a specific N_{1y}, say 12. In all plots, two different regions can be identified: $N_{2y} < 12$ and $N_{2y} > 12$. In the first region $N_{2y} < N_{1y}$, which means that the second element is not resolved as good as the first element, hence, the maximum error occurs in the second element. In this region, the maximum error decreases as N_{2y} is increased. In the second region, N_{2y} is larger than N_{1y} and the maximum error shifts to the first element. The maximum error is expected to remain constant since the expansion order in the first element is kept constant (at 12 for the case we are discussing now). To summarize, we expect to see an exponential decay in the region $N_{2y} < N_{1y}$ and a constant error for $N_{2y} > N_{1y}$. The deviations from this behavior, as seen in Fig. 6, is due to the *consistency errors* introduced by the non-conforming formulations [2].

The minimum and maximum rules behave similar for IPM (minimum rule performing slightly better), and follow the expected behavior as seen from Figs. 6(c) and (d). For PMM, results for the minimum rule (Fig. 6(a)) are very similar to those of IPM. However, PMM with maximum rule exhibit large consistency errors and looses convergence. These results can be seen as generalizations of the *polynomial order incompatibility* problem studied in [2], where the relative importance of consistency and approximation errors is analyzed for pointwise matching and integral matching approaches. The authors in [2] have shown that the

maximum rule, when used with PMM (Fig. 6(b)), results in *unbounded consistency errors* for certain combinations of N_{1y} and N_{2y}.

4.3. Test 3: convergence on an h-type non-conforming mesh

This is a test similar to the previous one, but this time a three-element, h-type non-conforming mesh, shown in Fig. 5(b), will be used. Similar to the previous test, expansion orders in the x-direction are kept constant at 16, while expansion orders in the y-direction are varied.

Fig. 7 shows the convergence curves for this test. For h-type non-conformities, instead of maximum and minimum rules, we use long rule with PMM and short rule with IPM. Let us consider the curve obtained with IPM for $N_{1y} = 16$. Up to $N_{2y} = 12$, the error decays exponentially. Maximum error occurs inside one of the small elements. After $N_{2y} > 12$ maximum error shifts to the big element, i.e. element 1, and the error stays constant because the expansion order of element 1 is kept constant. Similar behavior is obtained for other values of N_{1y}. Curves for PMM deviate from the straight line of spectral convergence in the interval $N_{2y} < N_{1y}$. Compared to IPM, PMM requires higher expansion orders to get the same level of error. For $N_{2y} > N_{1y}$ errors for PMM stay constant with values slightly lower than the corresponding IPM cases. However, in a physical problem it is unlikely to employ small elements with expansion orders (N_{2y}, N_{3y}) larger than that of the large element (N_{1y}). Due to the switch between the long and short rules between the PMM and IPM, these two methods do not use the same number of degrees of freedom. Therefore, one needs to be careful comparing errors obtained by PMM and IPM on h-type non-conforming meshes.

4.4. Test 4: eigenvalue analysis of the unsteady diffusion equation

In this section, we will analyze the eigenvalue spectrum of the unsteady diffusion equation using two-element p-type, and three-element h-type non-conforming meshes. Unsteady diffusion equation is given by

$$\frac{\partial \theta}{\partial t} - \nabla^2 \theta = 0. \tag{26}$$

After a semi-discrete formulation, the global discrete system of $\dot{\theta} = M^{-1} D\theta$ is obtained, which can be put into the following eigenvalue problem:

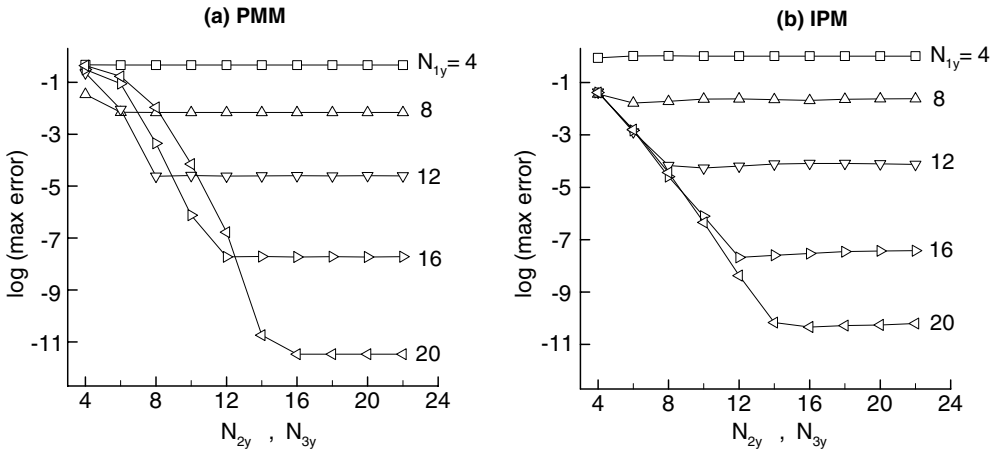

Fig. 7. Convergence curves obtained for the diffusion equation (Test 3). Three-element h-type non-conforming mesh is used for (a) PMM with long-rule and (b) IPM with short rule.

$$(M^{-1}D - \lambda I)\phi = 0, \tag{27}$$

where λ and ϕ are the eigenvalues and corresponding eigenvectors, respectively. M and D are the mass and diffusion matrices. All the boundaries are taken to be Dirichlet type.

Fig. 8 shows the growth of maximum eigenvalues with the expansion order. Fig. 8(a) is for a conforming mesh. The straight line has a slope of two, suggesting that the maximum eigenvalue increases linearly with the square of the expansion order, i.e. $|\lambda|_{\max} \sim \mathcal{O}(N^2)$. This trend agrees with that of the global spectral methods [12]. Similar trends are obtained for p-type and h-type non-conforming meshes. In Fig. 8(c), eigenvalues for IPM are slightly higher than those of PMM, because IPM uses the short rule resulting in more degrees of freedom. Note that for every case shown in Fig. 8, all the eigenvalues are real and negative. Therefore, non-conformities do not bring any instability problems for the diffusion operator, if one uses absolutely stable implicit schemes, such as Crank–Nicolson.

5. Convection equation

In this section, we will study the unsteady linear convection equation, starting with the eigenvalue spectra obtained with different kinds of non-conforming interfaces and formulations.

5.1. Test 5a: eigenvalue analysis of the unsteady convection equation on a p-type non-conforming mesh

In this test, we will analyze the eigenvalue spectrum of the convection operator using the four-element mesh shown in Fig. 5(c). Unsteady convection equation is given by

$$\frac{\partial \theta}{\partial t} + \mathbf{u} \cdot \nabla \theta = 0, \tag{28}$$

where $\mathbf{u}$ is a two-dimensional velocity field. For simplicity, we take the velocity field to be in the x-direction with a magnitude of 1. Dirichlet conditions on the top and bottom boundaries, and periodic conditions on the left and right boundaries are used. After a semi-discrete formulation, Eq. (28) gives the global discrete system of $\dot{\theta} = -M^{-1}A\theta$, which can be put into the following eigenvalue problem

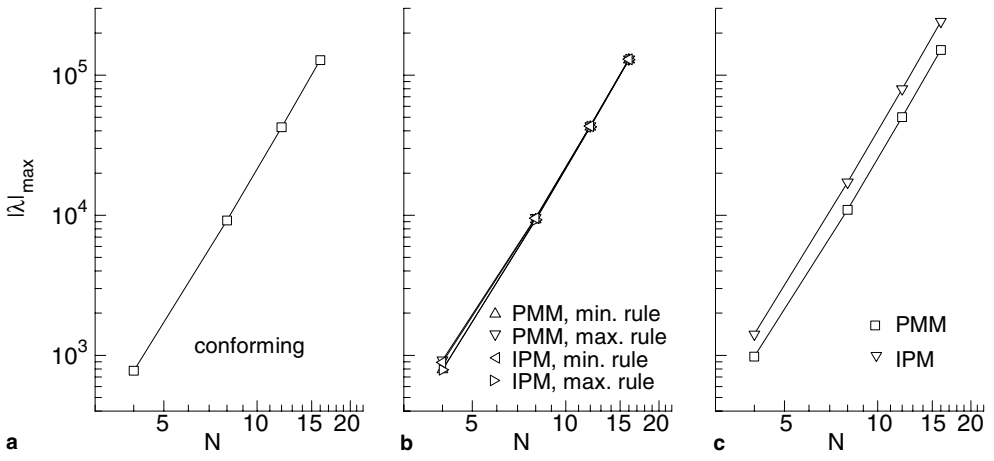

Fig. 8. Maximum eigenvalues for the unsteady diffusion equation (Test 4) using: (a) conforming mesh with same expansion order in both elements in both directions, (b) p-type non-conforming mesh with $N = N_1 = N_{2x}$ and $N_{2y} = N + 2$ and (c) h-type non-conforming mesh with same expansion order in all elements in both directions.

$$(-M^{-1}A - \lambda I)\phi = 0, \tag{29}$$

where A is the convection matrix.

Eigenvalue spectra for Test 5a are shown in Fig. 9. Identical results are obtained for PMM and IPM, so this figure will be referred without making a distinction between PMM and IPM. As seen from Fig. 9(a), conforming configurations result in all imaginary eigenvalues, as expected for the convection equation. In case of p-type non-conformities, both minimum and maximum rules result in eigenvalues with symmetric real parts. Real parts of the eigenvalues are larger for the maximum rule. We want to note that our eigenvalue results are similar to those presented in [21], where Ronquist studied the stability characteristics of convection dominated flows on grids with p-type non-conforming elements. However, he used PMM and IPM only with the minimum and maximum rules, respectively. Therefore, the differences in the eigenvalue spectrum were attributed to the PMM and IPM techniques. However, our results for p-type non-conforming elements show that these differences are due to use of the minimum and maximum rules, and they are induced by the "consistency errors". In Section 5.5, we will show that these consistency errors result in stability problems in solution of time-dependent problems, even if one utilizes a fully coupled space–time formulation.

We will continue by solving Test 5a using various orders of expansions to understand the relationship between the maximum real part of the eigenvalues $Re(\lambda)_{max}$, and the expansion order N. (This is similar to Test 4 that was performed for the diffusion operator.) Results are shown in Fig. 10. Behaviors of the minimum and maximum rules are similar. $Re(\lambda)_{max}$ increases with increased expansion order N, making the problem numerically more difficult to solve.

5.2. Test 5b: eigenvalue analysis of the unsteady convection equation on an h-type non-conforming mesh

The previous test considered p-type non-conformities. In this test, we study the eigenvalue spectrum of the convection operator using the four-element, h-type non-conforming mesh shown in Fig. 5(d). Similar to the previous case, top and bottom boundaries are Dirichlet type and right and left boundaries are periodic.

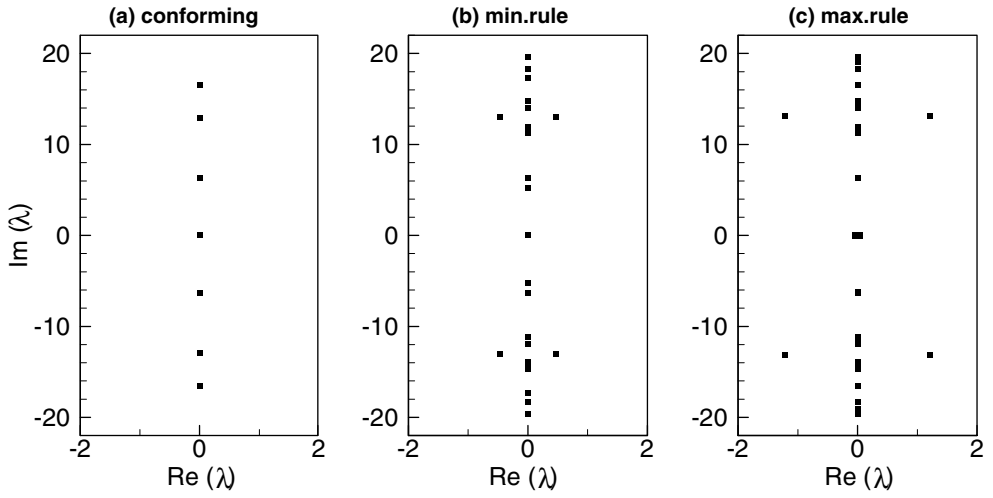

Fig. 9. Eigenvalue spectra for unsteady convection equation (Test 5a). Using: (a) conforming mesh, (b) p-type non-conforming mesh with minimum rule and (c) p-type non-conforming mesh with maximum rule. For conforming cases $N = 4$ is used in all elements. For non-conforming cases, expansion orders of $N_1 = N_2 = 4$ and $N_3 = N_4 = 5$ are used. In parts b and c, IPM and PMM give identical results.

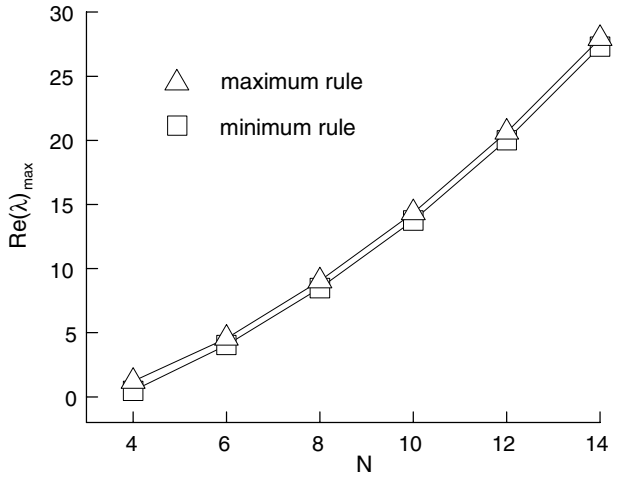

Fig. 10. Maximum real part of the eigenvalues for unsteady convection equation on a p-type non-conforming mesh (Test 5a) using the maximum and minimum rules. Expansion orders of $N_1 = N_2 = N$ and $N_3 = N_4 = N + 1$ are used. IPM and PMM give identical results.

Eigenvalue spectra for Test 5b are shown in Fig. 11. Unlike p-type non-conformities, results for PMM and IPM are different, because the former uses the long rule while the latter uses the short rule. Eigenvalues obtained with IPM are spread more on the real axis with larger real parts. Fig. 12 shows the relationship between the maximum real part of the eigenvalues $Re(\lambda)_{\max}$, and the expansion order N. Behavior of PMM is similar to the one obtained for the p-type refinement (Fig. 10). $Re(\lambda)_{\max}$ for IPM increases more rapidly than that of the PMM.

5.3. Test 6: unsteady convection equation on a conforming mesh

In the last two sections, we studied the eigenvalue spectrum of the convection operator for non-conforming interfaces. Now we will study the convergence characteristics of the pure convection equation, focusing

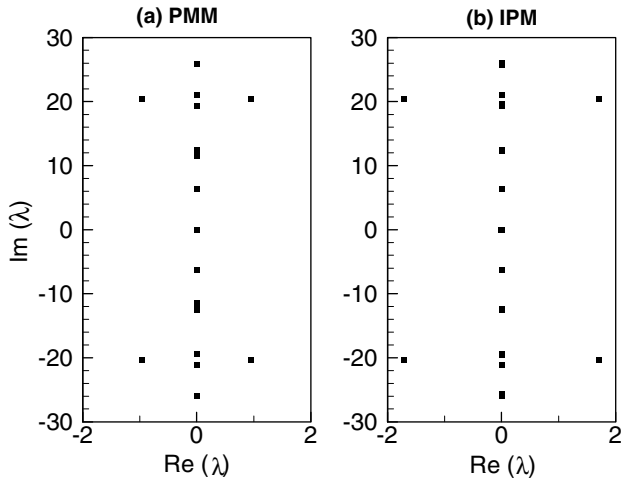

Fig. 11. Eigenvalue spectra for unsteady convection equation on an h-type non-conforming mesh (Test 5b). $N = 4$ used in all elements.

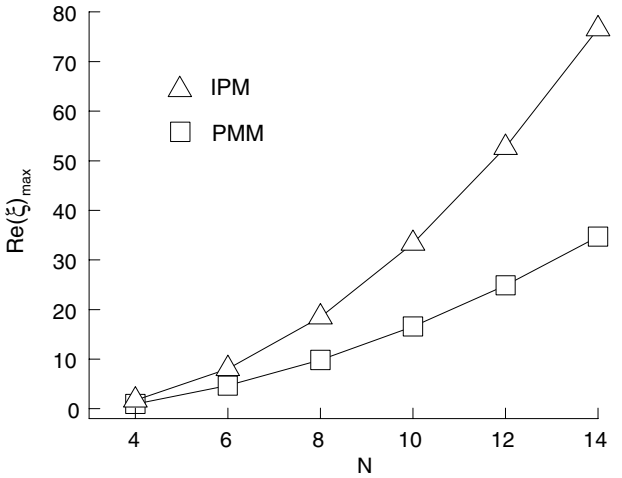

Fig. 12. Maximum real parts of the eigenvalues for unsteady convection equation on an h-type non-conforming mesh (Test 5b) using PMM and IPM. Expansion orders of N are used in each element.

on the effects of the positive real eigenvalues on time integration. Consider the following two-dimensional unsteady convection–diffusion equation

$$\frac{\partial\theta}{\partial t} - \alpha\nabla^2\theta + \frac{\partial\theta}{\partial x} = f \quad \text{on } \Omega \in [0,1]\times[0,1]. \tag{30}$$

For a zero force function, and the initial condition of

$$\theta(x,y,0) = \sin(2\pi x)\sin(\pi y),$$

the analytical solution is given by

$$\theta_{\text{exact}} = \sin(2\pi(x-t))\sin(\pi y)\mathrm{e}^{-5\pi^2\alpha t}, \tag{31}$$

where α is the constant diffusivity. To obtain an unsteady convection equation, we take $\alpha = 0$. Solution for this problem is a modified sine wave traveling in the positive x-direction. We use the four-element meshes shown in Figs. 5(c) and (d). On the top and bottom boundaries, exact solution is specified as Dirichlet boundary conditions. Left and right boundaries are periodic. Time integration is done by the Crank–Nicolson scheme, with a time step of 0.0002.

Let us start solving this problem with a fully conforming four-element mesh, using same expansion order in all elements and in both x and y-directions. Note that we are solving a pure convection problem with zero diffusivity. Fig. 13(a) shows the time history of errors for various expansion orders. Error levels decrease exponentially as expansion order is increased from $N = 4$ to $N = 8$. Small time step of 0.0002 results in errors dominated by space discretization, which accumulate slightly as time progresses. All three cases are stable.

5.4. Test 7: unsteady convection equation on a p-type non-conforming mesh

Let us repeat the previous test with expansion orders of $N_1 = N_2 = N$, $N_3 = N_4 = N + 2$ so that there will be p-type non-conforming interfaces. PMM with the maximum rule will be used. Note that IPM gives the same results as PMM and minimum rule differs only slightly from the maximum rule (see Figs. 9 and 10). Fig. 13(b) shows the time history of errors for various expansion orders. Only the case for $N = 4$ runs successfully for six cycles of the sine wave. Cases for $N = 6$ and $N = 8$ becomes unstable after

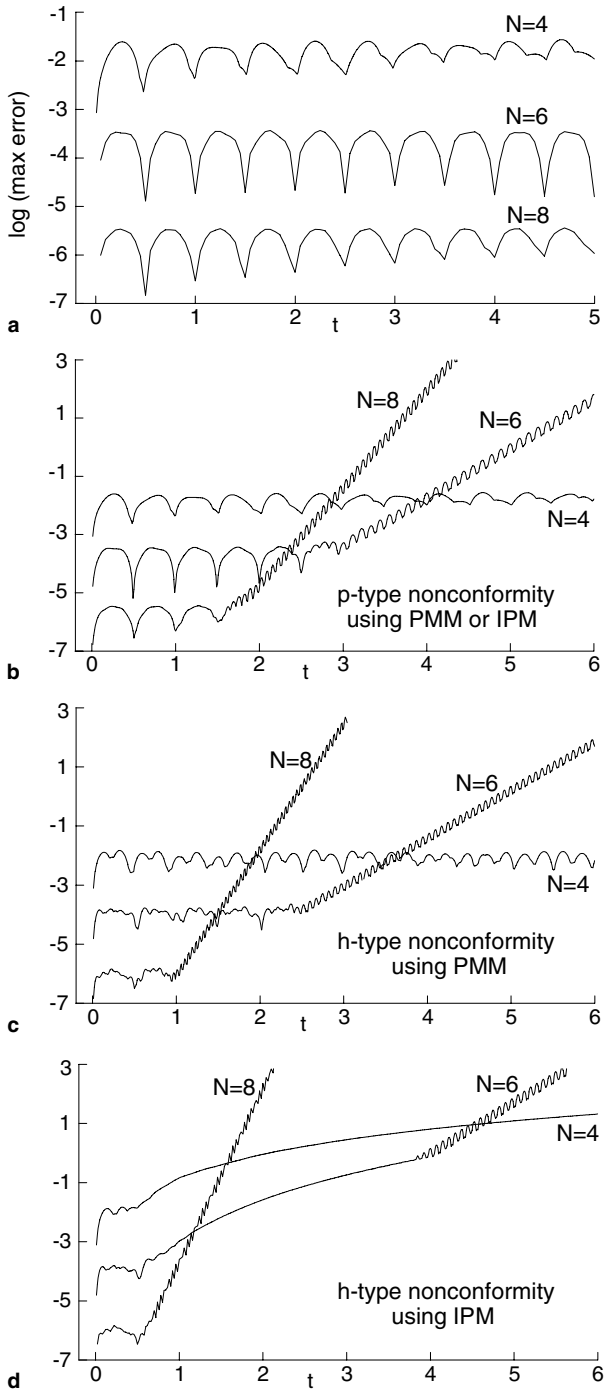

Fig. 13. Time evolution of error for unsteady convection equation. (a) Test 6: Conforming mesh with all four elements having the same expansion order N is used. (b) Test 7: p-type non-conforming interfaces are generated by using expansion orders of $N_1 = N_2 = N$, $N_3 = N_4 = N + 1$. (c,d) Test 8 using PMM and IPM, respectively. All four elements use the same expansion order. $t = 1$ corresponds to one cycle of the sine wave.

couple of cycles. Eigenvalues with positive real parts, introduced by the non-conforming formulation, are responsible for these blow-ups. The rate at which the error increases for $N = 8$ is larger than that of for $N = 6$. These error growth rates are directly related to the maximum positive real part of the eigenvalues (see Fig. 10).

5.5. Test 8: unsteady convection equation on an h-type non-conforming mesh

We will repeat this test using the h-type non-conforming, four-element mesh shown in Fig. 5(d). Same expansion order will be used in all elements. Figs. 13(c) and (d) show the time history of the errors for various expansion orders, for PMM and IPM, respectively. PMM results are very similar to the results of the previous test shown in Figs. 13(c) and (d). This is expected because of the similarity between the maximum eigenvalue results shown in Figs. 10 and 12. For IPM, instabilities setup earlier and errors increase with higher slopes. This behavior can be explained by Fig. 12, which shows higher positive eigenvalues for IPM compared to PMM. Even the case $N = 4$ is giving problems with IPM.

In the last three tests (6, 7, 8), a semi-discrete formulation with Crank–Nicolson time integration is used. Crank–Nicolson scheme is an absolutely stable scheme, with the stability region covering the whole 2nd and 3rd quadrants of the eigen-plane. But non-conforming formulations produce eigenvalues with positive real parts, which are responsible for the blow-ups. Additional consistency errors due to the non-conforming formulations are causing convergence problems. To validate further that this is a consistency problem, we repeated all three test cases using a fully coupled space–time formulation (instead of the previously used semi-discrete formulation). Similar to the spatial discretization, Lagrange interpolation functions based on GLL points are used for time discretization. Although the coupled formulation practically has no time stability restrictions, we obtained the same results. Therefore, we conclude that for pure convection problems, consistency errors due to the non-conforming formulations result in positive real eigenvalues, which makes these formulations *impractical* for *pure convection problems*.

Ronquist investigated convection-dominated viscous flows using both the pointwise matching and integral projection methods on p-type non-conforming grids [21]. He examined numerical stability of non-conforming spectral elements using convective and skew-symmetric forms of the convection operator. For convection-dominated viscous flows, he has shown different convergence characteristics based on the flow direction (whether the flow is from low-order to high-order elements, or vice versa), spatial and temporal (explicit versus implicit) discretization of the convection operator, and the use of PMM versus IPM. His study also included the eigenvalue spectra for various forms of the convection operator for non-conforming elements, which are qualitatively similar to our results presented in this section. Despite these limitations, Ronquist was able to obtain spectral convergence for Navier–Stokes equations using implicit time-stepping schemes, while explicit schemes were not quite successful even for $Re \leqslant 200$ flows [21]. Based on this experience, Ronquist concluded that implicit time-integration for Navier–Stokes equations on non-conforming elements are imperative for stability of PMM or IPM. We must reemphasize that numerical instabilities for *pure convection equation* will be observed regardless of the time integration scheme, as demonstrated in this section. Nevertheless, Ronquist's work has shown that physical diffusion due to the viscous terms may lead to stable Navier–Stokes solutions. Based on this, we first investigate the convergence characteristics of convection–diffusion equation for non-conforming formulations, and then analyze several Navier–Stokes test cases.

5.6. Test 9: convergence of the unsteady convection–diffusion equation

In the previous sections, we considered the pure convection problem. Now we will study the generalized convection–diffusion equation given by Eq. (30) with a non-zero diffusivity. Same traveling wave problem will be solved, exact solution of which is given by Eq. (31). Diffusivity is taken to be $\alpha = 0.01$. The four-

element meshes shown in Figs. 5(c) and (d) with periodic side boundaries will be used to study fully conforming, p-type non-conforming and h-type non-conforming cases.

For the conforming case, all four elements have expansion orders N. For the p-type non-conforming case, elements 1 and 2 have expansion orders N, and elements 3 and 4 have expansion orders $N + 2$. For the h-type non-conforming case, all elements have expansion order $N_x = N$ in the x-direction, elements 1 and 4 have expansion orders $N_y = N$, and elements 2 and 3 have expansion orders $N_y = 2$ in the y-direction. Convergence results are shown in Fig. 14. As given by Eq. (31), the analytical solution decreases exponentially by time, and so is the error. In order to circumvent this, we normalized the error by dividing it with $e^{-5}\pi^2\alpha t$. Crank–Nicolson scheme with a time step of 0.0002 is used for time integration. All four cases shown in Fig. 14 ran successfully for 10 cycles (first 5 is plotted), providing spectral convergence upon increasing the expansion order. The added diffusion is enough to shift all the eigenvalues to the left eigen-plane (in other words, enough to suppress the consistency errors), resulting in successful solutions. For the p-type non-conforming cases (b and c), maximum rule results in larger errors, although it uses more degrees of freedom. The difference between minimum and maximum rule is more apparent for lower expansion orders, especially with PMM. For the h-type non-conforming case PMM and IPM provides very similar results.

6. Solutions of the incompressible Navier–Stokes

Incompressible fluid flow is governed by the Navier–Stokes equations (written using the primitive variables)

$$\frac{\partial \mathbf{v}}{\partial t} + (\mathbf{v}\cdot\nabla)\mathbf{v} - \nu\nabla^2\mathbf{v} + \nabla p = \mathbf{f}, \tag{32a}$$

$$\nabla\cdot\mathbf{v} = 0, \tag{32b}$$

where $\mathbf{v}$ is the velocity vector, p is the pressure, ν is the kinematic viscosity and $\mathbf{f}$ is the body force vector. For simplicity, we assume that the density is equal to 1. We solved these equations using the Uzawa method [14,22] on a semi-staggered mesh, where velocities and pressures are calculated at Gauss–Lobatto–Legendre and Gauss–Lobatto points, respectively [7,22]. Unsteady problems are formulated using the semi-discrete approach, with fully implicit Crank–Nicolson time integration. Two test problems, oscillatory flow in a two-dimensional channel and steady Kovasznay flow, are studied to compare the convergence characteristics of PMM and IPM for both p-type and h-type of non-conformities. Finally, two-dimensional lid-driven cavity flow at $Re = 1000$ is investigated, and the results are verified with the data published in the literature.

6.1. Oscillatory flow in a two-dimensional channel

Consider the flow between two parallel plates, driven harmonically in time with a non-dimensional pressure gradient of the following form:

$$\frac{\partial p}{\partial x} = -Ae^{-it}, \tag{33}$$

where A is the pressure gradient amplitude and $i = \sqrt{-1}$. Velocity profile for this flow is given by [17]

$$u(y,t) = \mathrm{Real}\left\{ iAe^{-it}\left[1 - \frac{\cos\left(\frac{(i+1)}{\sqrt{2\beta}}y\right)}{\cos\left(\frac{(i+1)}{2\sqrt{2\beta}}\right)}\right]\right\}, \tag{34}$$

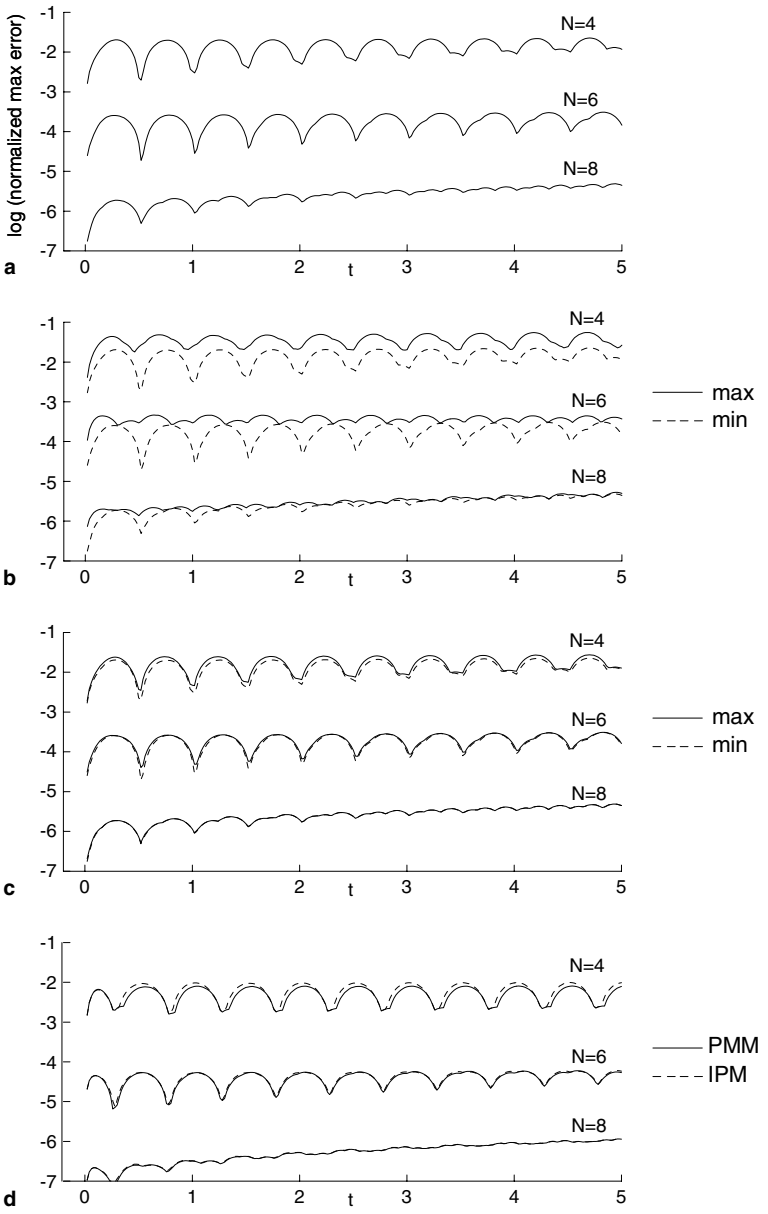

Fig. 14. Time evolution of error for unsteady convection–diffusion equation with $\alpha = 0.01$ (Test 9). Using: (a) conforming mesh, (b) p-type non-conforming mesh with PMM, (c) p-type non-conforming mesh with IPM and (d) h-type non-conforming mesh. Note that error is normalized by dividing it with $\exp(-5\pi^2\alpha t)$ to eliminate error reduction due to the diffusion of the signal.

where y is the cross channel distance normalized by the channel height. For time periodic flows, Womersley number (β) acts like a dynamic Reynolds number and determines the shape of the velocity profile. Fig. 15 shows the velocity profiles at various instances during a cycle for $\beta = 1$ and $\beta = 10$ flows. Quasi-steady flow behavior is observed for $\beta = 1$, while the Richardson's annular effect is present for $\beta = 10$. Here, we will study this problem for a Womersley number of 10, using the following three strategies

(a) *Conforming*. Four-element mesh shown in Fig. 5(c) is used (with a different range in the y-axis, $-0.5 < y < 0.5$). In the y-direction, same expansion order N_y is used for all elements. Since the flow is not changing in the x-direction, a low-order expansion $N_x = 3$ is used for all elements. This is also true for the following cases.
(b) *p-type non-conforming*. Same four-element mesh is used. Elements 1 and 4 have expansion orders N_y, and elements 2 and 3 have expansion orders $N_y + 2$.
(c) *h-type non-conforming*. Geometrically non-conforming four-element mesh shown in Fig. 5(d) is used. Elements 2 and 3 have expansion orders N_y, and elements 1 and 4 have expansion orders $N_y + 4$.

Exact solution at time zero is provided as the initial condition and the Navier–Stokes equations are integrated in time for 10 cycles. All cases run without any stability problems, with the errors shown in Fig. 16. Spectral convergence is obtained for all cases. For the p-type non-conforming cases, minimum rule performs better than the maximum rule, despite its use of lesser degrees of freedom than that of the maximum rule. These findings are in agreement with the results of the diffusion operator study given previously (in Fig. 6). For the h-type non-conforming case, PMM performs better than IPM for a given expansion order. This is expected because PMM utilizes more degrees of freedom, due to its use of the short rule.

6.2. Kovasznay flow

The streamlines of Kovasznay flow resemble low Reynolds number flow past an array of cylinders as shown in Fig. 17(a). It is an analytical solution to the Navier–Stokes equations, given by

$$\begin{aligned} u &= 1 - e^{\lambda x}\cos(2\pi y), \\ v &= \lambda/2\pi e^{\lambda x}\sin(2\pi y), \\ p &= 0.5(1 - e^{\lambda x}), \end{aligned} \tag{35}$$

where $\lambda = 0.5/\nu - (0.25/\nu^2 + 4\pi^2)^{0.5}$ and $\nu = 1/40$. Kovasznay flow is a popular test problem for high-order methods [13,14]. Similar to the previous test problem, we will perform conforming, p-type non-conforming and h-type non-conforming solutions, as follows:

(a) *Conforming*. Eight element mesh shown in Fig. 17(b) is used. Same expansion order N is used in all elements.
(b) *p-type non-conforming*. Same eight element mesh is used. Elements 1, 3, 5, 7 has expansion orders N, whereas elements 2, 4, 6, 8 has expansion orders $N - 2$. Only the maximum rule is tested.
(c) *h-type non-conforming*. Six element mesh shown in Fig. 17(c) is used. All elements has expansion order N, except elements 3 and 6 has expansion orders $N + 4$ in the y-direction.

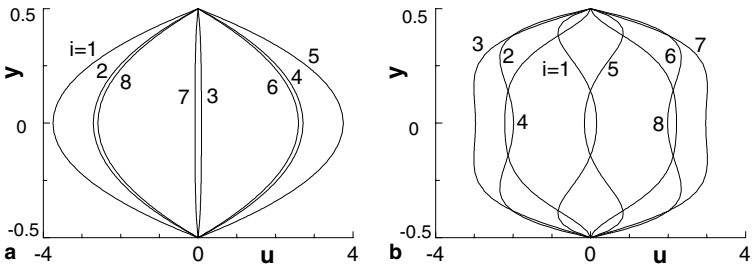

Fig. 15. Analytical solution of the velocity profiles at various times during a cycle for (a) $\beta = 1$, (b) $\beta = 10$ flow. Index i represents time within a period of the oscillations ($t = (i - 1)/8\tau$).

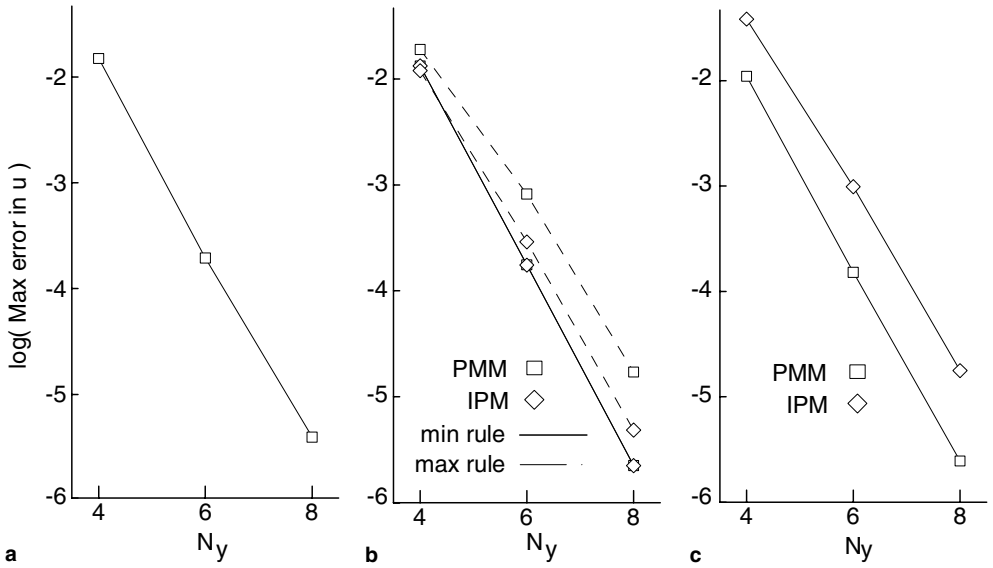

Fig. 16. Convergence results for the solution of the oscillatory flow in a channel for: (a) conforming, (b) p-type non-conforming and (c) h-type non-conforming cases. $N_x = 3$ for all elements in all cases.

Analytical solution is specified at all boundaries. Fig. 18 shows convergence results obtained from the steady Navier–Stokes solver. This time, maximum error is plotted against the square root of total number of degrees of freedom (ndf), including both velocity and pressure. Non-conforming solutions use multiple expansion order, therefore in order to provide a fair comparison of different solutions on a single plot ndf is used instead of N. Taking the square root of ndf ensures that the exponential convergence appears as a straight line on a log–lin graph. As seen from the figure, all three strategies result in spectral convergence. Similar to the previous case, when we use maximum rule with p-type non-conformity IPM performs better than PMM. For h-type non-conformity case, PMM and IPM results are practically the same.

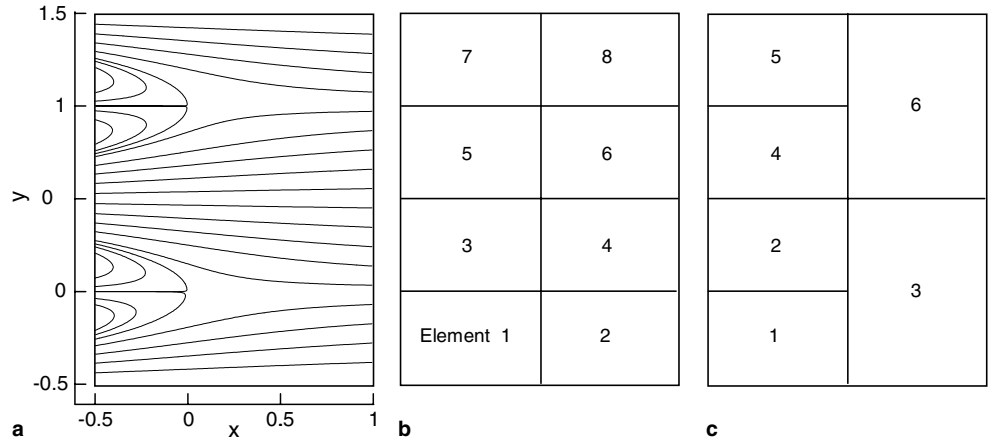

Fig. 17. Streamlines for the exact solution of the Kovasznay flow and two-different meshes used for the Kovasznay flow problem.

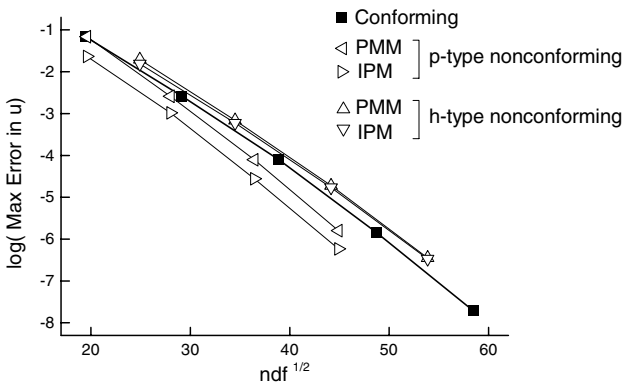

Fig. 18. Convergence results for different solutions of the Kovasznay flow. Maximum rule is used for the p-type non-conforming case. ndf is the total degrees of freedom including both the velocity and pressure fields.

6.3. Lid-driven cavity flow

Lid-driven cavity problem has a simple geometry and it is a classical Navier–Stokes test case. The problem geometry and boundary conditions are such that the top wall is moving in the tangential direction with a velocity of $u = -1$, while all other walls are stationary. Although this problem does not have a closed form analytical solution, it has been studied extensively, and many highly accurate benchmark results are available [1,5,23]. The challenging aspect of this problem is the singularities at top corners, which make the problem difficult for high-order formulations.

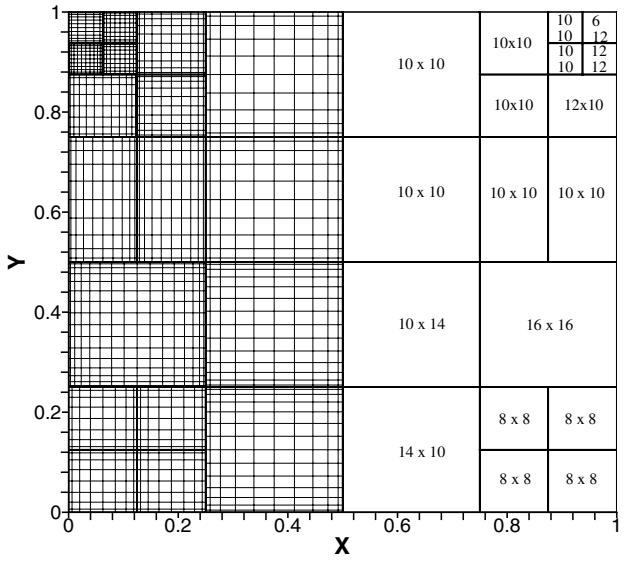

Fig. 19. Mesh used for the lid-driven cavity problem at $Re = 1000$. The left half of the figure shows the elements (thick-lines) and the collocation points (intersection of thin lines). The right half of the figure shows the element expansion order used in each element. The mesh is symmetric with respect to the $x = 0.5$ line.

The purpose of this study is twofolds: First we want to demonstrate that we can simultaneously utilize h- and p-type non-conformities for a realistic test-case. Second, we want to demonstrate that the consistency problems reported for pure convection equation are not observed for Navier–Stokes problems at relatively high Reynolds numbers.

We performed a series of simulations for Reynolds number 1000 flow, utilizing the mesh shown in Fig. 19. The mesh is symmetric with respect to $x = 0.5$ line. The figure shows elements with bold lines and the collocation points are shown in the left half of the figure by the intersection of thin lines. The right half of the figure shows polynomial expansions used in x- and y-directions. We have employed various levels of h- and p-type non-conformities, as shown in the figure. The top-right and top-left corners utilize 6×12 elements. Unlike other researchers, who employed "singularity substraction" methods to achieve spectral convergence [1,5,23], we deliberately under-resolved the corner-singularity regions of the flow. Our objective here is to demonstrate the "scientific accuracy" (maximum error of 1%) of our solution, since spectral convergence can not be obtained without subtracting the corner singularities [1,5,23]. In Fig. 20, we

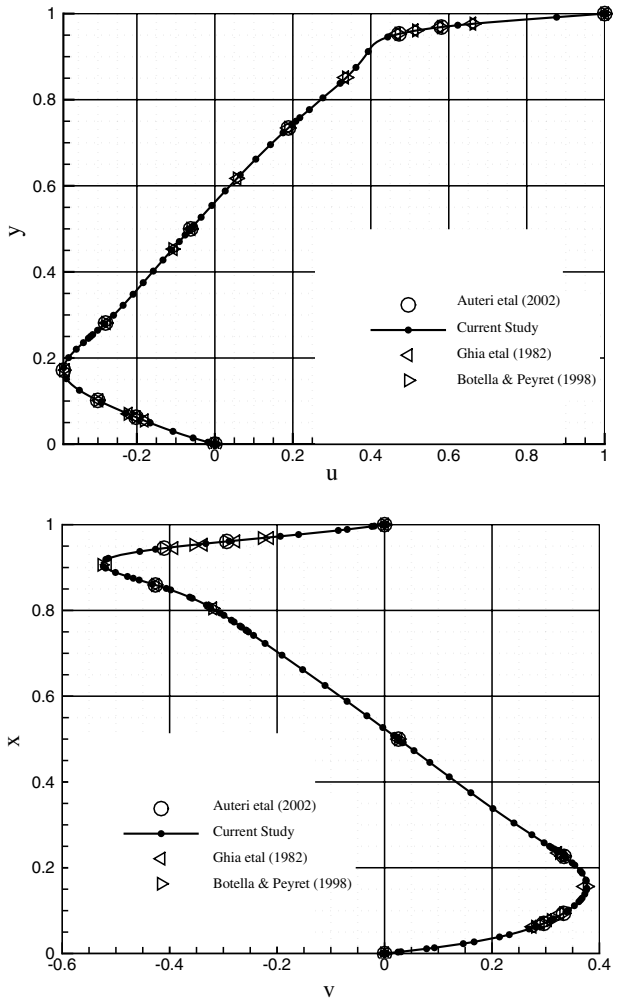

Fig. 20. Top: streamwise (u) velocity distribution along the $x = 0.5$ line. Bottom: cross-flow (v) velocity distribution along the $y = 0.5$ line. The results are compared with the spectral solutions in [1,5], and finite difference solutions in [9] at $Re = 1000$.

present the streamwise (u) and cross-flow (v) velocity profiles at $x = 0.5$ and $y = 0.5$ lines, respectively. The results are obtained by solution of the *steady* Navier–Stokes equations using the Uzawa algorithm. The non-linear terms require iterative solutions, where 60 iterations were necessary to reduce the velocity and pressure residuals below 1×10^{-12}. In Fig. 20, we also present comparisons of our solution with spectral solutions of [1,5], who employed ''singularity substraction'', and the finite difference solution of [9]. Our results in the figure successfully match the published data. The collocation points used in our simulations match the collocation points used in [1,5] only at $(x, y) = (0.5, 0.5)$. Therefore, we could do point-wise comparisons only at (0.5, 0.5), where we match the spectral solutions with singularity subtraction up to four significant digits using the current mesh resolution (Fig. 19). We believe this test case successfully demonstrates that the consistency problems for pure convection equation are not observed for the Navier–Stokes equations, at least up to $Re = 1000$.

7. Summary and conclusions

In this paper, we presented a comparative study of the pointwise matching and integral projection methods for both p- and h-type non-conforming grids. Although PMM and IPM are the two most popular non-conforming formulations, existing literature mostly concentrates on the PMM or IPM individually, and do not include the vast number of possibilities and rules that can be applied to handle hp non-conforming elements. In our study, we presented the PMM and IPM algorithms with step-by-step implementation details. Particularly, we considered the minimum-, maximum-, short- and long-rules, and addressed their convergence characteristics and eigenvalue spectra for steady and unsteady diffusion, convection, and convection/diffusion equations.

For several cases, non-conforming formulations resulted in consistency errors, in agreement with the previous work [2,21]. Solution of the diffusion equation exhibited *polynomial order incompatibility* for PMM with the maximum rule on p-type non-conformities. PMM with the minimum rule and IPM with both minimum and maximum rules provided acceptable results. For h-type non-conformities, PMM exhibited loss of spectral convergence, and it did not perform as well as the IPM.

For the unsteady convection equation, PMM and IPM with p-type non-conformities have identical eigenvalue spectra. Consistency errors for p-type non-conformities shift some of the eigenvalues into the positive real eigenplane. We correctly attributed this shift to the use of maximum or minimum rules, and not to the use of PMM or IPM (Fig. 9). The situation is similar for h-type non-conformities, where positive real components of the eigenvalues are larger for IPM (due to the use of the short-rule) compared to the PMM (which uses the long-rule). Positive real components of the eigenvalues result in numerical instabilities for solution of the unsteady convection equation using non-conforming grids. Coupled space–time formulations were also used to correctly identify the source of these problems to be the consistency errors coming from the non-conforming formulations.

Consistency errors were not observed for the convection–diffusion problems. Small ''physical'' diffusion seemed to eliminate the convergence problems induced by the positive real components of the eigenvalues, observed for the unsteady convection operator using non-conforming grids. Encouraged by this result, we studied the steady and unsteady incompressible Navier–Stokes equations using the Uzawa technique. Spectral convergence was demonstrated utilizing both PMM and IPM on test problems with known analytical solutions. Although the maximum rule used more degrees of freedom, it did not perform as well as the minimum rule. The PMM and IPM provided comparable results, with no distinct advantage of one over the other.

Finally, elimination of the consistency errors with small physical diffusion is an indication that the consistency errors *may* become important for convection dominated flows with diminishing viscosity. This may induce a maximum Reynolds number limit for the simulations. Although our results for the

two-dimensional lid-driven cavity problem at $Re = 1000$ did not exhibit any limitations, we plan to explore and report such limitations in future studies.

Acknowledgments

This material is based upon work supported by the National Science Foundation under Grant No. 0306622. A.B. would like to thank his student, Mr. Ho Jun Kim, for detailed lid-driven cavity simulations.

References

[1] F. Auteri, N. Parolini, L. Quartapelle, Numerical investigation of the stability of singular driven cavity flow, J. Comput. Phys. 183 (2002) 1–25.
[2] C. Begue, C. Bernardi, N. Debit, Y. Maday, G.E. Karniadakis, C. Mavriplis, A.T. Patera, Nonconforming spectral element-finite element approximations for partial differential equations, Comp. Meth. Appl. Mech. Engrg. 75 (1989) 109–125.
[3] C. Bernardi, Y. Maday, C. Mavriplis, A.T. Patera, The Mortar element method applied to spectral discretizations, in: T.J. Chung, G.R. Karr (Eds.), Finite Element Analysis in Fluids, Seventh International Conference on Finite Element Methods in Flow Problems, UAH Press, Hunstville, 1989.
[4] C. Bernardi, Y. Maday, A.T. Patera, A new nonconforming approach to domain decomposition: The Mortar element method, in: H. Brezis, J.L. Lions (Eds.), Nonlinear Partial Differential Equations and Their Applications, Piman and Wiley, 1992.
[5] O. Botella, R. Peyret, Benchmark spectral results on the lid-driven cavity flow, Comput. Fluids 27 (1988) 421–433.
[6] C. Canuto, M.Y. Hussaini, A. Quarterino, T.A. Zang, Spectral Methods in Fluid Dynamics, Springer, New York, 1988.
[7] R.-Y. Chang, C.-H. Hsu, A variable-order spectral element method for incompressible viscous flow simulation, Int. J. Numer. Meth. Engrg. 39 (1996) 2865–2887.
[8] D. Funaro, A. Quarteroni, P. Zanoli, An iterative procedure with interface relaxation for domain decomposition methods, SIAM J. Numer. Anal. 25 (1988) 1213–1236.
[9] U. Ghia, K.N. Ghia, C.T. Shin, High-*Re* solutions for incompressible flow using the Navier–Stokes equations and a multigtid method, J. Comput. Phys. 48 (1982) 387–411.
[10] D. Gottlieb, S.A. Orszag, Numerical Analysis of Spectral Method: Theory and Applications, SIAM, Philadelphia, 1977.
[11] A.K. Gupta, A finite element for transition from a fine to a coarse grid, Int. J. Numer. Meth. Engrg. 12 (1978) 35–45.
[12] R.D. Henderson, G.E. Karniadakis, Unstructured spectral element methods for simulation of turbulent flows, J. Comput. Phys. 122 (1995) 191–217.
[13] G.E. Karniadakis, M. Israeli, S.A. Orszag, High-order splitting methods for the incompressible Navier–Stokes equations, J. Comput. Phys. 97 (1991) 414–443.
[14] G.E. Karniadakis, S.J. Sherwin, Spectral/hp Element Methods for CFD, Oxford University Press, New York, 1999.
[15] D.A. Kopriva, A conservative staggered-grid Chebyshev multidomain method for compressible flows. II: A semi-structured method, Technical Report, Institute for Computer Applications in Science and Engineering, Number TR-96-15, 1996.
[16] C. Lacour, Y. Maday, Two different approaches for matching nonconforming grids: The Mortar element method and the FETI method, BIT 37 (1997) 720–738.
[17] L.D. Landau, E.M. Lifshitz, Course of Theoretical Physics, Fluid Mechanics, vol. 6, Pergamon Press, New York, 1987.
[18] Y. Maday, A.T. Patera, Spectral element methods for the Navier–Stokes equations, in: A.K. Noor (Ed.), State of the Art Surveys in Computational Mechanics, ASME, New York, 1989, pp. 71–143.
[19] A.T. Patera, A spectral element method for fluid dynamics, laminar flow in a channel expansion, J. Comput. Phys. 54 (1984) 468–488.
[20] J.N. Reddy, An Introduction to the Finite Element Method, McGraw-Hill, New York, 1993.
[21] E.M. Ronquist, Convection treatment using spectral elements of different order, Int. J. Numer. Meth. Fluids 22 (1996) 241–264.
[22] C. Sert, Nonconforming Formulations with Spectral Element Methods, Ph.D. Thesis, Mechanical Engineering Department, Texas A&M University, 2003.
[23] W.W. Schultz, N.Y. Lee, J.P. Boyd, Chebyshev pseudospectral method of viscous flows with corner singularities, J. Sci. Comput. 4 (1989) 1–24.
[24] C.T. Tsai, B.A. Szabo, A constraint method – a new finite element technique, NASA Technical Memorandum, NASA, TM X-2893 (1973), 551–568.